applied sciences

MDPI

Article

Numerical Study on the Bending Performance of Steel-Ribbed Composite Slabs for Substations

Lin Li [1], Yong Liu [1], Zhenzhong Wei [1], Yunan Jiang [1], Haomiao Chen [2], Yu Zhang [2,*], Chen Liu [2], Kunjie Rong [2] and Li Tian [2]

[1] Shandong Electric Power Engineering Consulting Institute Co., Ltd., Jinan 250013, China
[2] School of Civil Engineering, Shandong University, Jinan 250061, China; kunjierong@sdu.edu.cn (K.R.); tianli@sdu.edu.cn (L.T.)
* Correspondence: yu_zhang@sdu.edu.cn

Abstract: This study investigates the bending behavior of steel-ribbed composite slabs for a 500 kV substation project in China through numerical simulation. The unidirectional bending performance of the slab was first analyzed and validated against theoretical calculations. After that, the bidirectional bending performance of double-spliced and triple-spliced composite slabs were evaluated against the monolithic slab, followed by a parametric analysis to identify the influence of key factors. The results indicate that the steel-ribbed composite slabs feature high cracking strength, post-crack stiffness, bearing capacity, and commendable ductility under both unidirectional and bidirectional loading conditions. Under unidirectional loading, the ultimate capacity of the slab reaches 57–58 kN/m^2. Under bidirectional loading, the cracking load and bearing capacity of the dense-splicing composite slabs increase by more than 60% compared with unidirectional loading. Composite and monolithic slabs exhibit similar crack patterns and ultimate capacities under bidirectional loading; however, the presence of splicing joints results in a slight increase in the ultimate deflection of the double-spliced and triple-spliced composite slabs by 7.53% and 7.75% compared with that of the monolithic slab. The ratio of prestressing steel is identified as the most critical parameter for failure control, followed by the concrete strength. When the strength of the joint-connecting rebars exceeds 235 MPa and the diameter is greater than 4 mm, transversal force transfer across the joints is reliable. This paper provides valuable insights and practical guidance for the prefabricated construction of substations.

Keywords: steel-ribbed composite slab; prestressed concrete composite slab; bidirectional loading; prefabricated construction; substation

check for updates

Academic Editor: Francesco Tornabene

Received: 2 January 2025
Revised: 23 February 2025
Accepted: 24 February 2025
Published: 7 March 2025

Citation: Li, L.; Liu, Y.; Wei, Z.; Jiang, Y.; Chen, H.; Zhang, Y.; Liu, C.; Rong, K.; Tian, L. Numerical Study on the Bending Performance of Steel-Ribbed Composite Slabs for Substations. *Appl. Sci.* **2025**, *15*, 2876. https://doi.org/10.3390/app15062876

Copyright: © 2025 by the authors. Licensee MDPI, Basel, Switzerland. This article is an open access article distributed under the terms and conditions of the Creative Commons Attribution (CC BY) license (https://creativecommons.org/licenses/by/4.0/).

1. Introduction

To meet the growing demand for electricity in the process of urbanization, a series of power transmission projects has been launched in China under the guidance of the "West-to-East Power Transmission" strategy. Consequently, the scale and number of substations in China have also expanded continuously. Guided by policies advocating for "green, low-carbon, energy-saving, and environmentally friendly design", the concept of prefabricated structures has been vigorously promoted [1–4]. To date, several prefabricated substations have been completed and put into operation or are under construction nationwide [5–7]. In comparison with civil buildings, substation buildings feature large equipment loads and large spans, resulting in more stringent requirements for the floor systems.

Currently, research on prefabricated components for substations has mainly focused on enclosure walls and frame systems [8–10], with limited studies addressing floor systems. Liu et al. [11] performed theoretical and numerical analyses of prestressed steel pipe truss floor slabs based on previous experimental programs and further discussed the practical applications in real substation projects. The influence of grouting strength, steel pipe wall thickness, concrete strength grade, prestressed slab thickness, the number of prestressed tendons, and the prestress value on the unidirectional bending performance of prestressed steel pipe truss floor slabs is investigated. Yu et al. [12] further studied the influence of the "secondary force" of the prestressing tendons on the overall mechanical behavior of prestressed concrete steel pipe truss slabs. The results show that the "secondary force" effect reduces the cracking load of the composite slab and increases the maximum crack width. Huang et al. [13] conducted experiments to study the influences of rib details on the flexural behavior of concrete composite slabs with precast prestressed ribbed panels. The results show that composite slabs with rectangular ribbed panels and composite slabs with T-shaped ribbed panels can achieve the same flexural behavior as cast-in-place slabs. Liu et al. [14] proposed a prestressed concrete composite slab featuring inverted T-shaped ribs and investigated the impact of three different rib forms on the bending performance through experimental tests and numerical analysis. Hou et al. [15] further conducted four-point bending tests on twelve prestressed concrete composite slabs with inverted T-shaped concrete ribs and beams underneath to study the bending stiffness, ultimate load-bearing capacity, and failure modes. Karimipanah et al. [16] carried out an experimental study on the bending behavior of composite slabs with cold-formed profiled steel sheeting, finding that profiled steel sheeting behaves like tensile reinforcement beside the concrete slab, and the failure mode was concrete crushing. Lei et al. [17] investigated the thermal–mechanical coupling evaluation of the panel performance of a prefabricated cabin-type substation based on machine learning.

The studies mentioned above primarily focus on the unidirectional performance of floor slabs, with relatively few studies addressing composite slabs subjected to bidirectional loading. Wang et al. [18] conducted static load tests on four two-way concrete composite slabs and investigated the stress state at the joints. The results revealed that increasing the lap reinforcement length and cross-sectional height at the joints significantly enhanced the overall integrity and flexural capacity of the composite slabs. Li et al. [19] carried out bidirectional loading tests on laminated two-way slabs with L-shaped joints, conventional dense-splicing joints with additional reinforcement, and cast-in-place bidirectional slabs. The deflection, reinforcement strain, and crack development of the test slabs, as well as the force transmission mechanism at the joint, were analyzed. Cheng et al. [20] conducted stacking tests on dense-splicing composite slabs with steel-bar trusses measuring 3.6 m × 3.6 m and supported at four edges to study the ultimate capacity, failure modes, load transfer, and stiffness. The results indicate that the dense-splicing composite slabs with additional overlapped reinforcements crossing the joints can ensure reliable force transmission under bidirectional loading. However, the crack distribution as well as the stiffness is slightly different from the cast-in-place slabs. Chen et al. [21] proposed a new dense-splicing technique for two-way composite slabs using grooves and closed-ring reinforcement. The structural performance of the new type of joint was studied by full-scale tests and found to be basically the same as that of the cast-in-place slab.

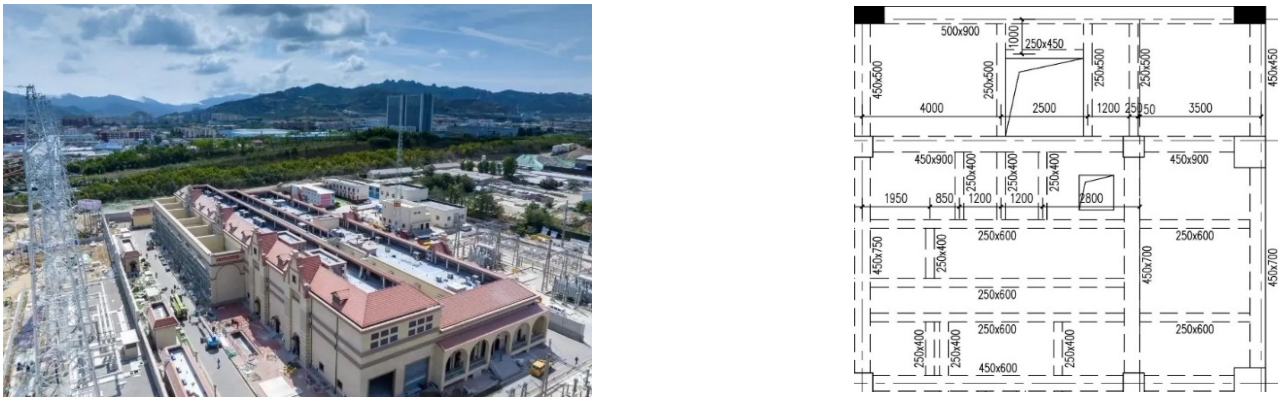
This study introduces a new type of prestressed concrete composite slab with steel ribs and explores its potential in applications of large-scale prefabricated substation construction. The paper begins by outlining the project background and design scheme of the floor slabs, followed by the finite element modeling of the composite slabs. Subsequently, the unidirectional bending performance of the composite slab along the direction of the

prestressed tendons is analyzed and the ultimate capacity is compared with theoretical calculations for validation. After that, double-spliced and triple-spliced composite slabs are analyzed to access their bidirectional performances followed by a parametric analysis to identify the influence of key factors.

2. Design Scheme of Steel-Ribbed Composite Slabs

2.1. Project Background

The Daocheng (Huangbuling) 500 kV substation, shown in Figure 1a, was upgraded from the original 220 kV substation. The introduction of new transformer equipment has increased the design floor loads to 34.2 kN/m^2, much higher than that for civil buildings. In order to meet the stringent requirements, the scheme of steel-ribbed composite slabs was adopted in the prefabricated construction. Meanwhile, a grid of inner beams was set beneath the floor slabs for enhancement. Figure 1b illustrates part of the structural layout plan for the 8.800 m floor. It can be seen that parts of the floors belong to one-way slabs. However, most floors enclosed by primary and secondary beams, where the ratio of the room's long side to short side is less than 2, will be subjected to bidirectional loading.



(**a**) (**b**)

Figure 1. Daocheng (Huangbuling) 500 kV substation. (**a**) Aerial view; (**b**) Layout plan for the 8.800 m floor (mm).

2.2. Design Parameters of Steel-Ribbed Composite Slabs

The steel-ribbed composite slabs feature higher stiffness and bearing capacity compared with other slab systems such as composite slabs with steel-bar trusses. The composite slab consists of the precast base slab with inverted T-shaped ribs and post-cast concrete, as shown in Figure 2. The inverted T-shaped rib has a concrete upper flange and a thin steel web. The design parameters of the steel-ribbed composite slab are described as follows.

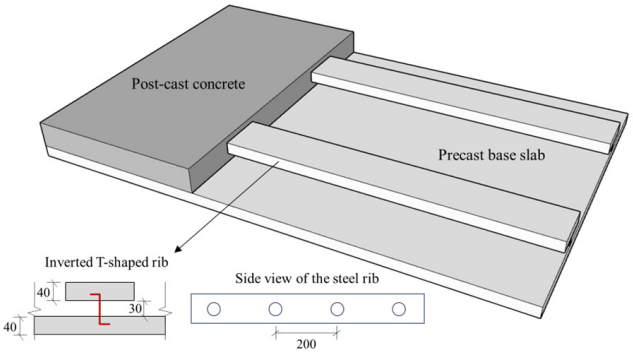


Figure 2. Illustration of the steel-ribbed composite slab (mm).

According to the Technical Specification for Prestressed Concrete Composite Slab with Steel Ribs (T/CECS 1289-2023) [22], the specified strength grades of the concrete for the precast base slab and the post-cast concrete layer should not be lower than C40 and C30, respectively. For the steel, the specified yield strength should not be lower than 235 MPa. Given that the design load for substations is high, the precast base slab and post-cast concrete layer both utilize C40 concrete, which has a cubic compressive strength of 40 MPa for a specimen measuring 150 mm × 150 mm × 150 mm. The steel ribs in the precast base slab are Z-shaped, with a thickness of 1 mm and a height of 67 mm, as depicted in Figure 2. The yield strength of the steel ribs is 235 MPa. Circular holes, spaced 200 mm apart, are arranged in the middle of the steel ribs. The upper end of each steel rib is embedded within a concrete flange that has a width of 150 mm and a thickness of 40 mm, while the lower end is anchored in the precast concrete slab. Prestressing steel (labeled as ① in Figure 3), composed of $A5^H$ 1570-grade stress-relieved spiral ribbed steel, is placed longitudinally in the precast concrete slab, aligned with the direction of the steel ribs. The controlling stress of the prestressing steel is 1100 MPa, 70 percent of the ultimate strength 1570 MPa. Steel bars of diameter C8, spaced at 150 mm (labeled as ③ in Figure 3), are oriented perpendicular to the direction of prestressing, possessing a yield strength of 400 MPa. At the ends of the slab, the arrangement of steel bars is intensified, labeled as ② in Figure 3. Longitudinal steel rebars of 2C6 (labeled as ④ in Figure 3) and transvers steel rebars of C6 spaced at 375 mm (labeled as ⑤ in Figure 3) are placed in the concrete flange of steel ribs. The slanted cut at the edge of the precast base slab, aligned with the direction of the parallel prestressing, measures 20 mm × 20 mm. The thickness of the precast base slab is 40 mm, increasing to 110 mm when including the ribs. The total thickness of the slab after composition is 130 mm. To investigate the impact of joint positioning following dense splicing under bidirectional loading, two sizes of precast base slabs—designated as A and B—have been developed, as shown in Figure 3. The size of slab A is 1650 mm × 2500 mm, with three steel ribs and 22 prestressing steels (ratio of 0.201%), and slab B measures 1100 mm × 2500 mm, with two steel ribs and 14 prestressing steels (ratio of 0.192%). The center distance between adjacent steel ribs in both slabs is 550 mm.

The manufacture cost of the steel-ribbed composite slab is slightly higher than that of other slab systems due to the consumption of more steel. However, the scheme is still cost-effective, benefitted by dense splicing in the prefabricated construction, which reduces the costs of formwork, support, and labor for wet joints on site. For bidirectional slabs after dense splicing, the position and number of splicing joints are critical. Two classical splicing configurations, i.e., double-spliced and triple-spliced, are studied here and compared with the cast-in-place monolithic slab, as shown in Figure 4. The dimensions of the bidirectional composite slabs are 3300 mm × 2500 mm. The double-spliced configuration has only one joint, but it is placed at the most unfavorable stress (mid-span) location, while the triple-spliced configuration incorporates two joints strategically located at third-point positions. Additional connecting rebars of C8 @ 200 mm, each with a full length of 3300 mm and through the circular holes in the steel ribs, are placed on the precast slab to enhance the transversal force transfer across the splicing joints.

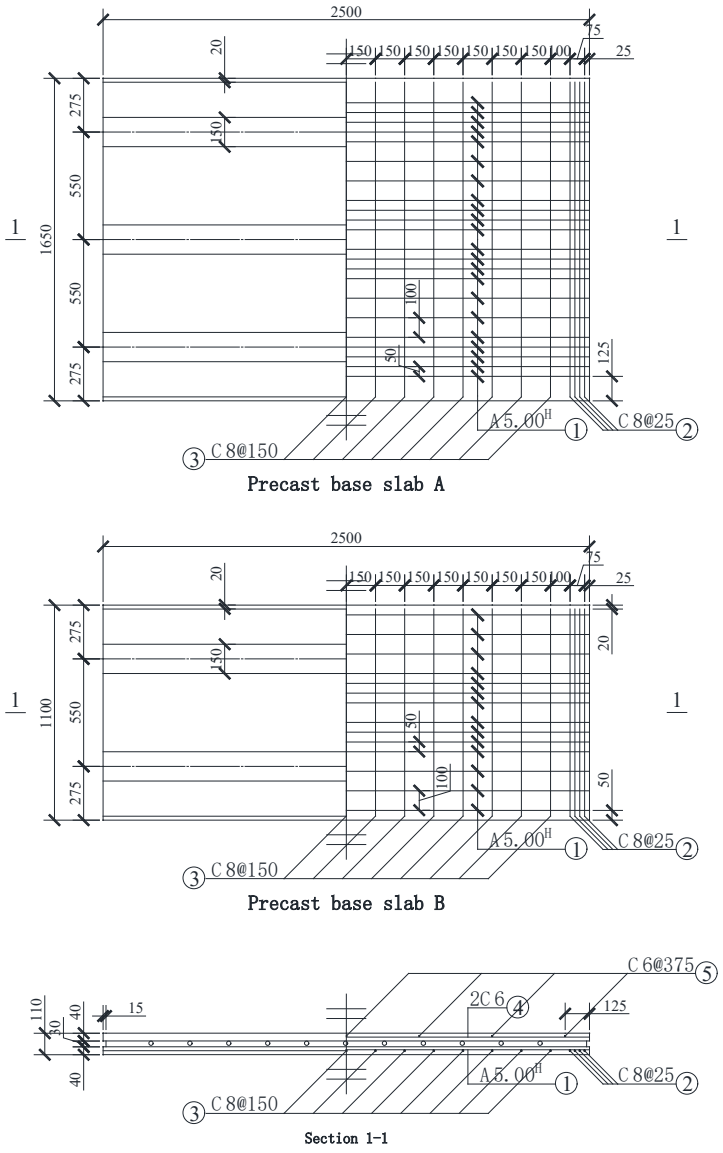


Figure 3. Detailed drawing of precast base slabs A and B (mm).

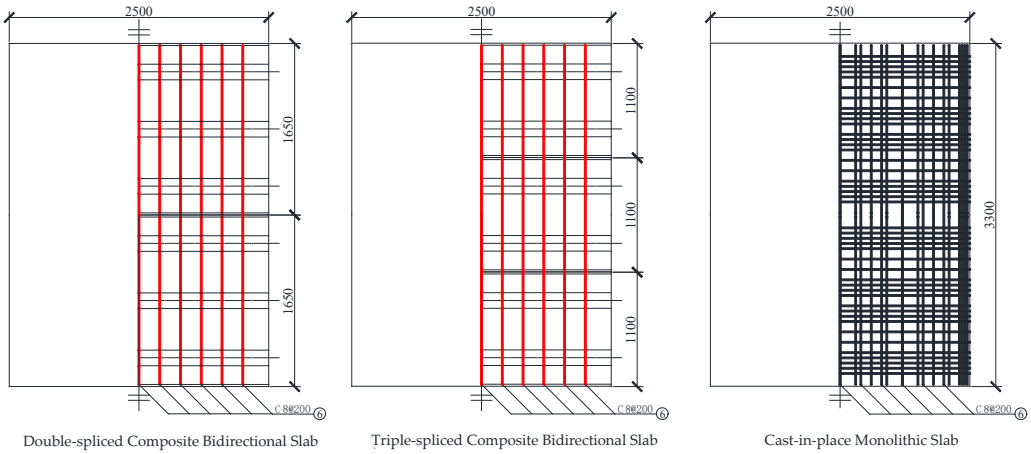


Figure 4. Double-spliced, triple-spliced, and cast-in-place monolithic slab (mm).

3. Finite Element Modeling

3.1. Basic Assumptions

The integrity of composite slabs is critical under loading, especially at the interfaces of the laminated (precast and post-cast) concrete layers. According to the experimental results [14], the existence of the inverted T-shaped ribs can increase the contact surface, making the laminated concrete layers work compositely. As a result, the following basic assumptions are made for the numerical simulation and analysis for simplicity:

1. The materials are assumed to be isotropic and homogeneous;
2. The relative slip between the laminated concrete layers is negligible, and the two layers work together.
3. Perfect bonding is assumed between the concrete and steel (rebars, prestressing steels, and steel ribs) without any relative slip.

3.2. Establishment of Finite Element Models

The finite element (FE) models of the composite slabs are established using the Abaqus software [23]. The concrete parts and steel ribs are modeled using solid elements C3D8R. The rebars and prestressing steel are modeled with truss elements T3D2. The material parameters for steel and concrete components are shown in Table 1.

Table 1. Material properties.

Component	Young's Modulus (MPa)	Poisson's Ratio	Yield Stress (MPa)
Prestressing steel	206,000	0.3	1570
Rebar	206,000	0.3	400
Steel rib	206,000	0.3	235
Concrete	32,500	0.2	2.4/26.8 [1]

[1] Cracking/ultimate compressive strength for concrete.

The constitutive model for concrete employs the concrete damage plasticity (CDP) model built into the Abaqus software, with the required parameters specified in Table 2. The dilation angle in the table describes the plastic strain due to shear stress after the elastic phase. The flow potential eccentricity is 0.1, which implies that the material has almost the same dilation angle over a wide range of confining pressure stress values. The parameter f_{b0}/f_{c0} is the ratio of biaxial to uniaxial compressive yield stresses, denoting the characteristics of the failure function. The viscosity parameter is employed in viscoplastic regularization equations to achieve convergence. These parameters define the material's behavior under different loading conditions and are crucial for the accurate simulation of concrete behavior. The responses of concrete to uniaxial loading in compressive and tensile behavior are shown in Figure 5a–d. It should be noted that creep and shrinkage effects in the concrete are not considered herein. For rebars and prestressing steels, the bilinear model is adopted to demonstrate elastic and plastic stages, as shown in Figure 5e,f. The reduction rate in the elastic modulus during the plastic stage is 0.01 of that in the elastic stage.

Table 2. Parameters of concrete damage plasticity.

Dilation Angle	Eccentricity	f_{b0}/f_{c0}	K	Viscosity Parameter
30	0.1	1.16	0.6667	0.005

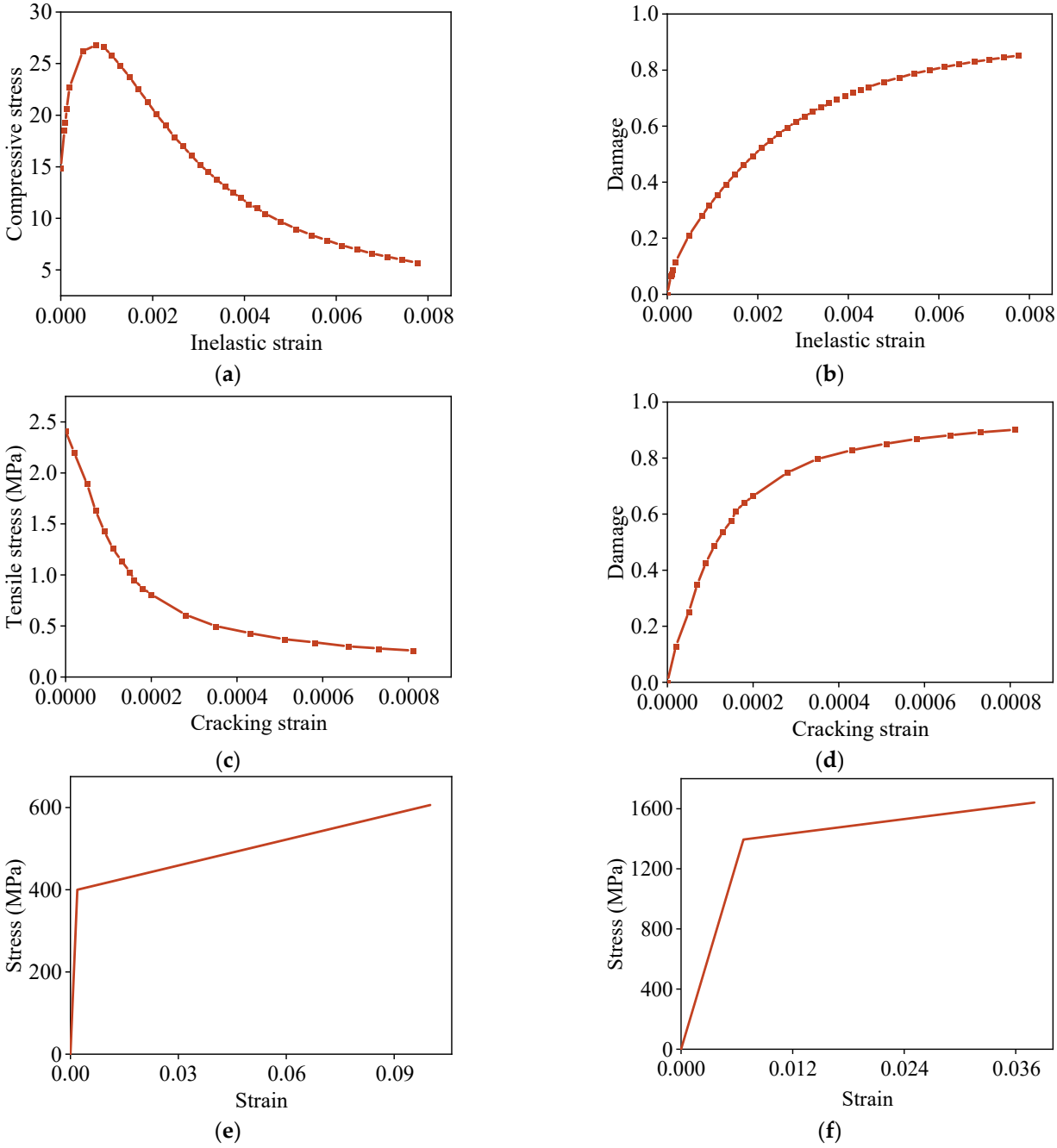


Figure 5. Constitutive models: (**a**) Response of concrete in compression; (**b**) Concrete compressive damage; (**c**) Response of concrete in tension; (**d**) Concrete tensile damage; (**e**) Response of rebar in tension; (**f**) Response of prestressing steel in tension.

The FE models of steel-ribbed composite slabs A and B are shown in Figures 6 and 7, respectively. The reinforcement (rebar and prestressing steel) is embedded in the precast base slab. The interaction between the precast base slab and the post-cast concrete layer is set as "tied" without any relative slip. Two strips of rigid cushion blocks are placed under the ends of the slab perpendicular to the direction of the steel ribs to prevent local failure. The reinforcement mesh size is approximately 20 mm. For the precast base slab and post-cast concrete layer, the mesh sizes are 20 × 20 × 20 mm and 20 × 20 × 22 mm, respectively, aligning with the reinforcement mesh size. The steel ribs and upper concrete flange are modeled with mesh sizes of 1 × 10 × 20 mm and 20 × 50 × 50 mm, respectively. A coarser mesh size of 50 × 50 × 50 mm is applied to the rigid cushion blocks. Simply

supported boundary conditions are defined along the centerline of the bottom surface of the cushion blocks.

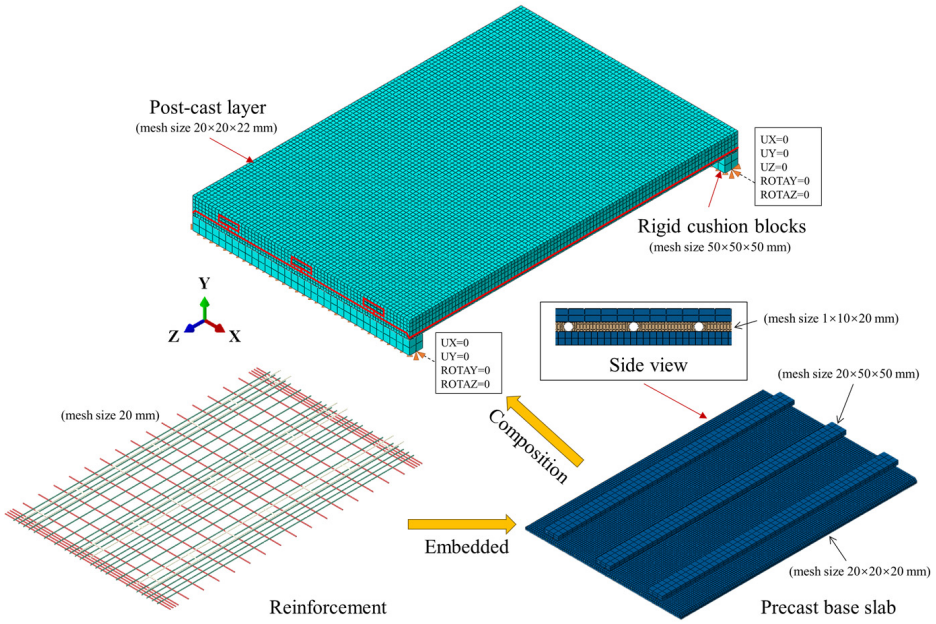


Figure 6. FE model of steel-ribbed composite slab A.

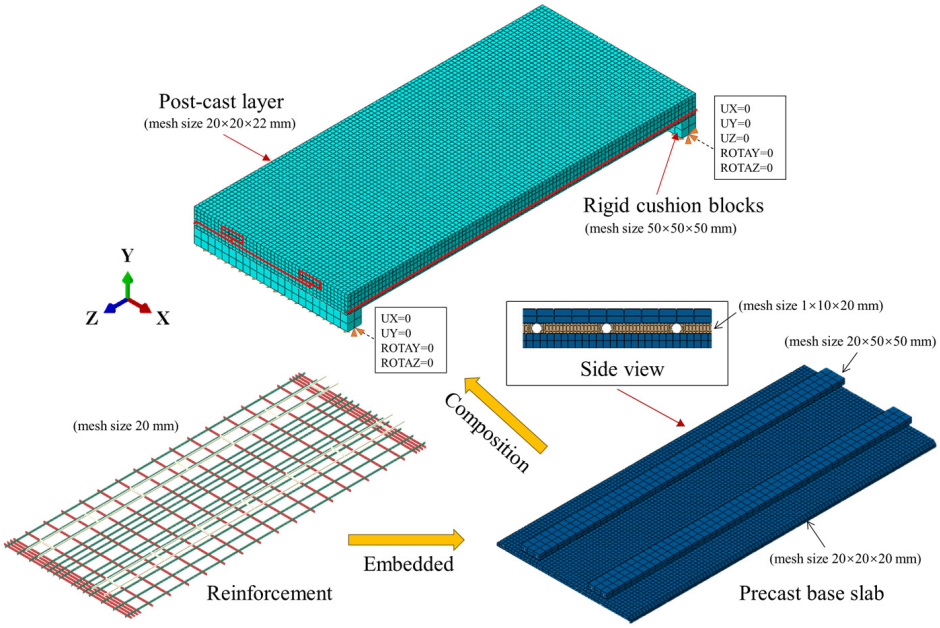


Figure 7. FE model of steel-ribbed composite slab B.

The FE models of the double-spliced, triple-spliced, and cast-in-place monolithic composite bidirectional slabs are shown in Figures 8–10, respectively. The joint of the spliced slabs is defined as "hard" contact and allows separation, with the tangential friction coefficient set to 0.8. Rigid cushion blocks are placed under the edges of the slab for bidirectional loading. Simply supported boundaries are set on the center line of the bottom surface of the four-sided cushion blocks.

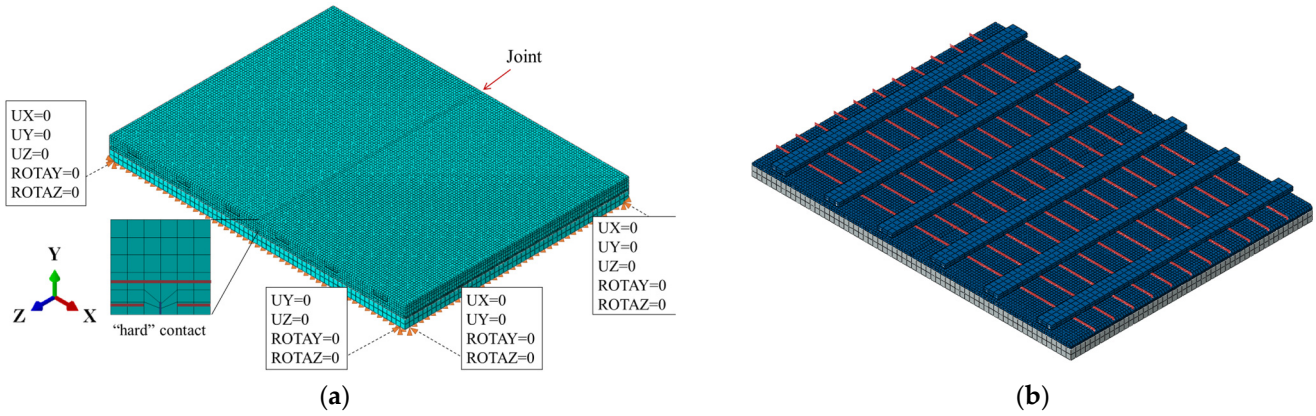


Figure 8. FE model of the double-spliced composite slab: (**a**) After composition; (**b**) Transverse joint-connecting rebars before composition.

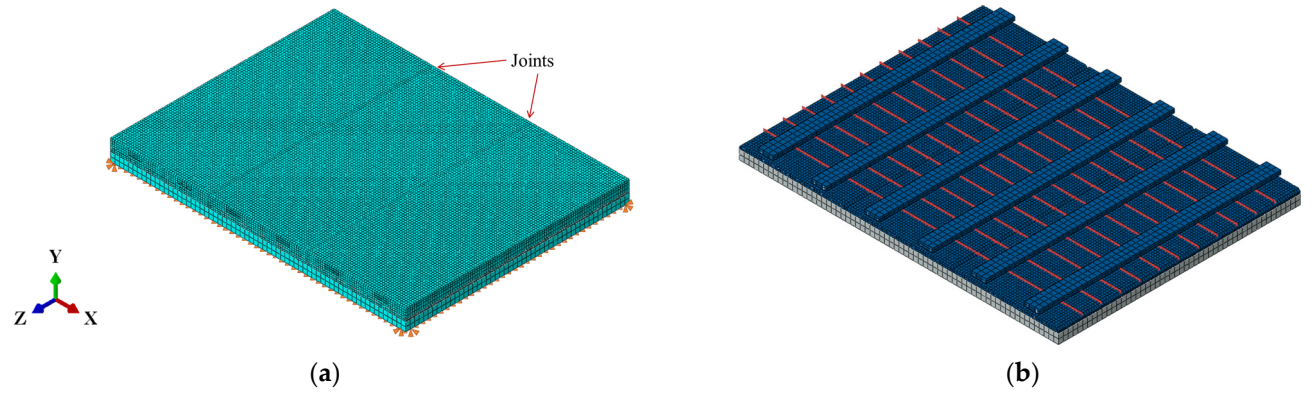


Figure 9. FE model of the triple-spliced composite slab: (**a**) After composition; (**b**) Transverse joint-connecting rebars before composition.

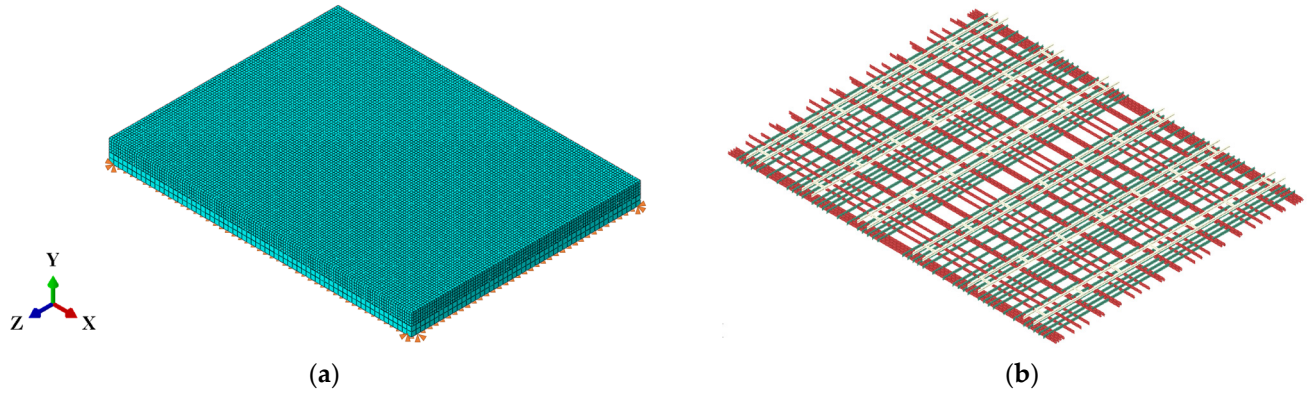


Figure 10. FE model of the cast-in-place monolithic slab: (**a**) After construction; (**b**) Reinforcement.

3.3. Validation of Finite Element Models

The experimental data from previous studies [14,24] were utilized to validate the aforementioned FE modeling approach. The comparison between test and FE results is presented in Figure 11, which also includes the key parameters of the specimens. Figure 11a demonstrates the unidirectional bending test of a simply supported precast base slab subjected to uniform loading. The FE model demonstrated excellent agreement with experimental results in terms of pre-cracking stiffness and bearing capacity, showing an average error of only 3%. In the post-cracking phase, the FE model exhibited slightly higher stiffness compared with the test results, with a maximum deviation of approximately

8%, leading to a smaller ultimate deflection. This discrepancy may be attributed to the assumption of perfect bonding between concrete and steel in the FE model, which is acceptable in simulation analysis. Figure 11b presents the load–deflection curves of the composite slab with a post-cast layer under four-point bending conditions. Also, the shape of the load–deflection curves obtained from the FE model was similar to the test result. The error of the cracking load or bearing capacity between the FE model and test was generally within 5%. Overall, the experimental data showed strong correlation with the finite element analysis, thereby validating the FE modeling methodology for subsequent numerical investigations.

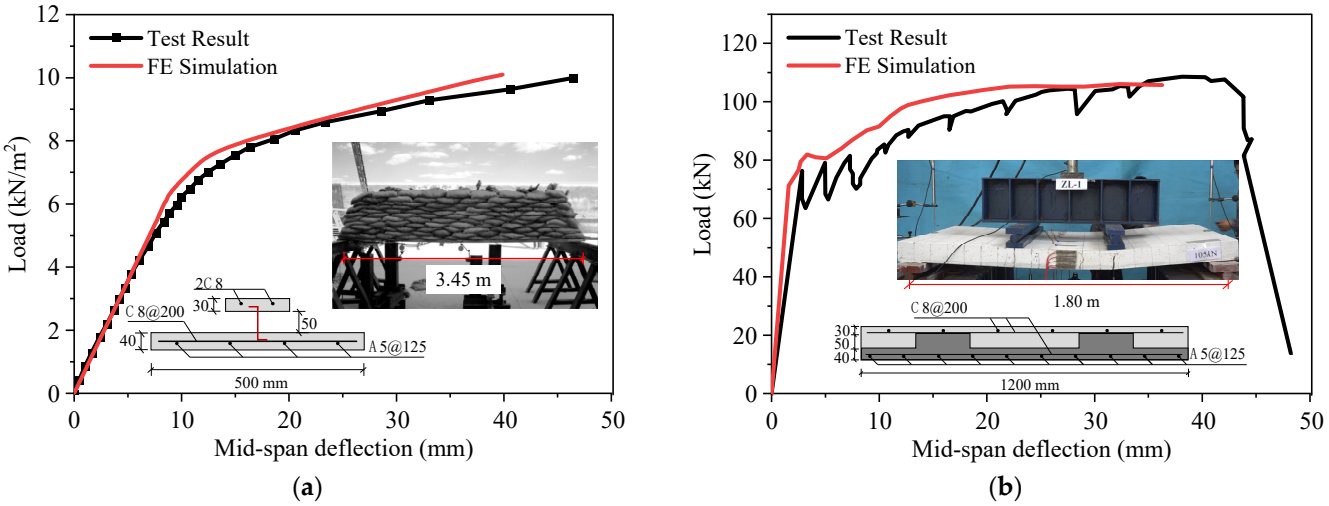


Figure 11. Comparison of load–deflection curves between test and FE results: (**a**) Uniform loading of the precast base slab [24]; (**b**) Four-point loading of the composite slab [14].

It is noteworthy that both the precast base slab and the composite slab exhibited typical flexural failure modes under unidirectional loading. The ultimate load-bearing capacity closely aligns with the theoretical calculations based on the Technical Specification for Prestressed Concrete Composite Slab with Steel Ribs (T/CECS 1289-2023) [22] and the Chinese Code for Design of Concrete Structures (GB 50010-2010) [25]. As a result, the code-based theoretical calculations of the flexural capacity can be employed as an alternative means for rapid verification of the FE model's rationality, as demonstrated in the following section.

4. Unidirectional Bending Performance of Composite Slabs

Gravity load is applied to simply supported composite slabs A and B with an increasing, uniformly distributed load applied to the slab surface. Given that the slabs are designed as balanced reinforced members, the yielding of the prestressing steel can be selected as the failure criterion. The static analysis results are as follows.

4.1. Results of Composite Slab A

Figure 12a,c,e illustrate the deflection of composite slab A, the distribution of cracks at the bottom surface, and the stress in the prestressing steel at the cracking load of 32.669 kN/m^2. It can be seen that cracks first appear at the mid-span perpendicular to the long edge of the slab, and they have a tendency to develop inward. The mid-span deflection is 1.266 mm, with the stress in the prestressed steel uniformly distributed and slightly greater than the tension control stress. Figure 12b,d,f show the corresponding behaviors at failure, correlating with an ultimate load of 58.268 kN/m^2. It can be observed that the cracks have fully developed at the bottom surface, uniformly distributed from

mid-span toward the near supports, and cracks appear at the steel ribs in the direction parallel to the long edge of the slab. Meanwhile, there are localized companion cracks along the direction of the steel ribs, indicating that the steel ribs play an important role in the longitudinal force transfer. At the failure moment, the prestressing steel reaches the yielding stress of 1570 MPa, and the mid-span deflection has increased to 17.52 mm.

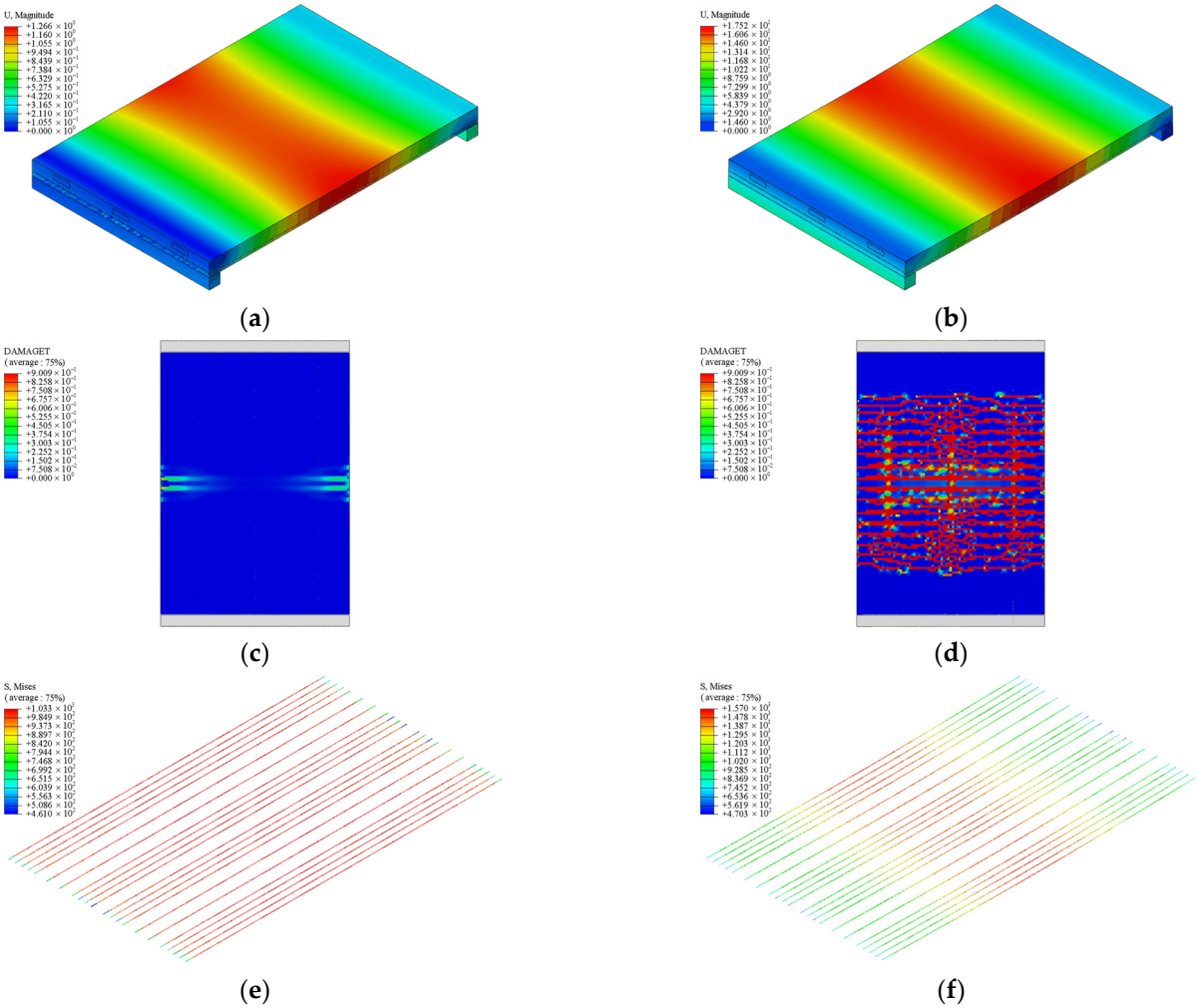


Figure 12. Analysis results of composite slab A under unidirectional loading: (**a**) Deflection at cracking; (**b**) Deflection at failure; (**c**) Initial bottom cracks at cracking; (**d**) Distribution of bottom cracks at failure; (**e**) Stress in prestressing steel at cracking; (**f**) Stress in prestressing steel at failure.

4.2. Results of Composite Slab B

Figure 13a,c,e show the deflection of composite slab B, the distribution of cracks at the bottom surface, and the stress in the prestressing steel at the cracking load of 31.827 kN/m^2. Similar to composite slab A, the initial cracks also appear at the mid-span of the slab, but they are more continuous in the transverse direction due to a greater span-to-width ratio. The mid-span deflection is 1.249 mm, slightly lower than that of composite slab A. The stress in the prestressed steel exhibits a uniform distribution of approximately 1033 MPa, which is the same as composite slab A. Figure 13b,d,f show the corresponding behaviors at failure, with an ultimate load of 57.409 kN/m^2. The cracking characteristics are basically consistent with slab A, with transverse cracks uniformly distributed from the mid-span toward the supports, and longitudinal cracks appearing near and along the steel ribs. The mid-span deflection at failure is 18.08 mm, and the prestressing steel has yielded.

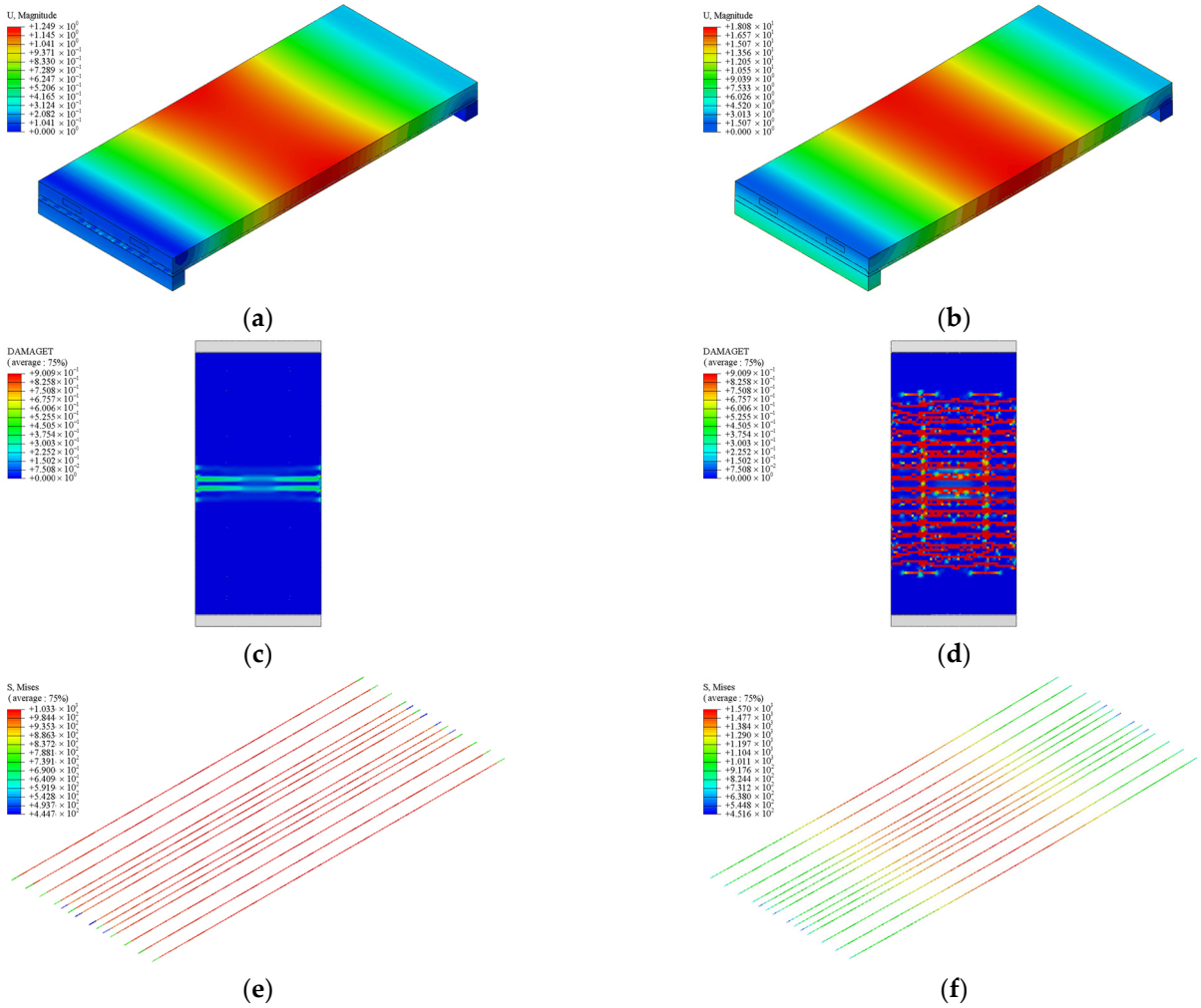


Figure 13. Analysis results of composite slab B under unidirectional loading: (**a**) Deflection at cracking; (**b**) Deflection at failure; (**c**) Initial bottom cracks at cracking; (**d**) Distribution of bottom cracks at failure; (**e**) Stress in prestressing steel at cracking; (**f**) Stress in prestressing steel at failure.

4.3. Discussion of Results

Figure 14 shows the load–deflection curves for composite slabs A and B, and both present typical two-stage load-bearing characteristics with the point of concrete cracking as the turning point. Before cracking, the composite slab is in the elastic stage, and the load–deflection curve is approximately a straight line. After cracking, the curves show a turning point, indicating a significant reduction in the slab's stiffness. As the load increases and cracks develop, the post-crack stiffness of the composite slab remains relatively stable until failure. Throughout this entire process, the composite slab exhibits commendable ductility. The stiffness and ultimate capacity of composite slab A are slightly greater than those of composite slab B, due to a marginally higher prestressing steel ratio in composite slab A compared with composite slab B.

The theoretical results of the flexural capacity using the codes [22,25] were also calculated here for reference and double-checked for the rationality of the numerical analysis. Composite slab A was taken as an example, with the calculation process outlined as follows:

The width and thickness of composite slab A is b = 1650 mm, H = 130 mm. The number of the prestressing steel is n = 22 with the diameter d = 5 mm and the yielding strength f_{py} = 1570 MPa. The concrete cover of the prestressing steel is c = 23 mm. The calculation span is $l_0 = 2500 - 50 \times 2 = 2400$ mm.

The effective depth of the section is

$$h_0 = H - c - d/2 = 130 - 23 - 5/2 = 104.5 \text{ mm}. \quad (1)$$

The area of reinforcement is

$$A_p = (n\pi d^2)/4 = (22 \times \pi \times 5^2)/4 = 431.969 \text{ mm}^2. \quad (2)$$

The relative height of the compression zone is

$$\xi = (A_p f_{py})/(f_c' b h_0) = (431.969 \times 1570)/(26.8 \times 1650 \times 104.5) = 0.147. \quad (3)$$

The section resistance moment coefficient is

$$\alpha_s = (1 - (1 - \xi)^2)/2 = (1 - (1 - 0.147)^2)/2 = 0.136. \quad (4)$$

The bending capacity of the section is

$$M = \alpha_s f_c' b {h_0}^2 = 0.136 \times 26.8 \times 1650 \times 104.5^2 = 6.567 \times 10^7 \text{ N·mm}. \quad (5)$$

The external uniformly distributed load is

$$q = (8 \times M)/(b {l_0}^2) = (8 \times 6.567 \times 10^7)/(1650 \times 2400^2) = 55.278 \text{ kN/m}^2 \quad (6)$$

Similarly, the external uniformly distributed load of composite slab B can be obtained as 52.955 kN/m^2. The errors between the theoretical calculations and the simulation results for slabs A and B are −5.13% and −7.76%, respectively. The theoretical calculations yield slightly lower values than those obtained from the FE models. This is likely due to the omission of the contribution from the steel ribs in the theoretical calculations. Overall, the FE analysis demonstrates a relatively high level of accuracy and can be reliably utilized for subsequent static analyses of bidirectional slabs.

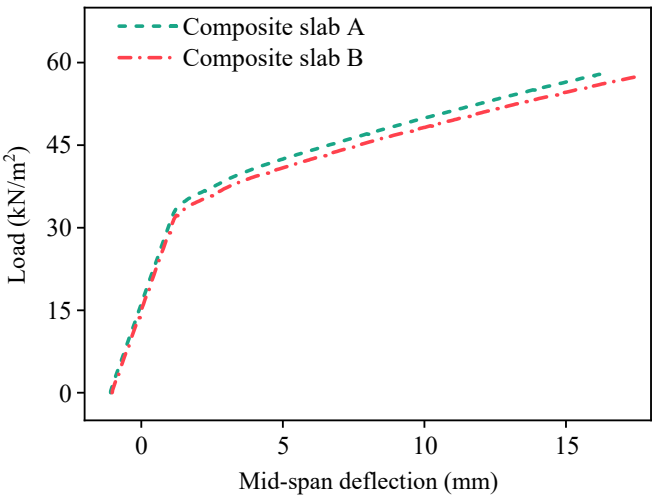


Figure 14. Load–deflection curves for steel-ribbed composite slabs at mid-span.

5. Bidirectional Bending Performance of Composite Slabs

For composite bidirectional slabs that are simply supported on all four edges, a gravity load combined with an increasing, uniformly distributed load on the slab surface is applied. The failure criterion employed in the analysis is also based on the yielding of the prestressing steel. The analysis results are as follows.

5.1. Double-Spliced Composite Bidirectional Slab

Figure 15a,c,e,g show the deflection of the double-spliced composite bidirectional slab, the distribution of cracks on the bottom surface, and the stress in the prestressing steel when cracking occurs. The cracking load is 53.701 kN/m^2, with a corresponding mid-span deflection of 1.276 mm. Initial cracks appear near the middle of the joint, with a tendency to develop in the transverse direction. The stress in the prestressed steel demonstrates a uniform distribution of approximately 1028 MPa. The stress in the transverse reinforcement is significantly higher at the joint than the other parts, with a maximum value of 51.56 MPa. Figure 15b,d,f,h depict the corresponding behaviors at the failure load of 101.299 kN/m^2, and the mid-span deflection increases to 14.85 mm. The cracks on the bottom surface exhibit a checkerboard pattern near the mid-span and extend diagonally toward the four slab corners, which follows a classical bidirectional cracking mode. The prestressing steel near the center of the slab has yielded, leading to the failure of the slab. For the transverse reinforcement, the stress of the joint-connecting rebars reaches a maximum value of 302.3 MPa, while the stress in the rebars of the precast slab remains relatively lower, about 200 MPa. This indicates that the transversal force is transferred through the joint-connecting rebars and subsequently to the regular rebars of the precast slab.

Figure 16a,b illustrate the load–stress curves for the prestressing steel and the joint-connecting rebar at the center of the slab. It can be observed that both load–stress curves are approximately linear before the concrete cracking. Due to the smaller thickness of the concrete cover, the prestressing steel exhibits greater efficiency under loading, resulting in a steeper curve compared with the joint-connecting rebar. When cracking occurs at a load of about 55 kN/m^2, the stress in the prestressing steel starts to develop rapidly. However, the load–stress curve begins to show a turning point at a lower load of 40 kN/m^2, indicating that the joint tends to open up before concrete cracking. As the load continues to increase to 80 kN/m^2, the stress development of the joint-connecting rebar accelerates, signifying a dramatic expansion of the joint width.

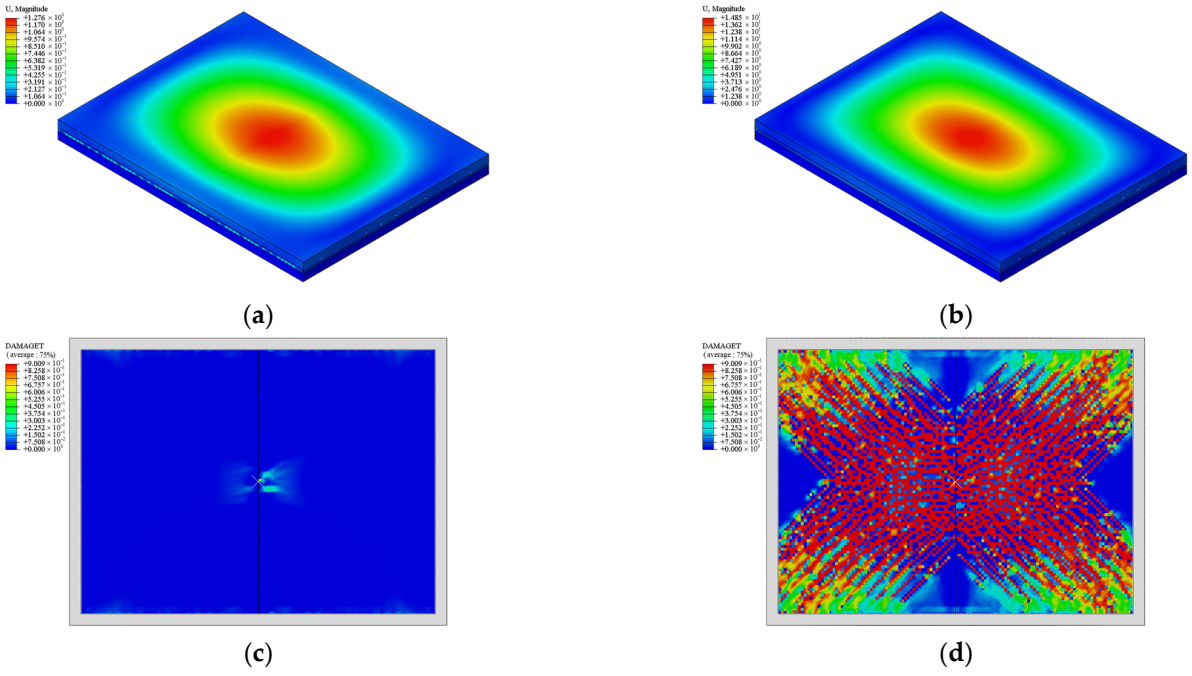


Figure 15. *Cont.*

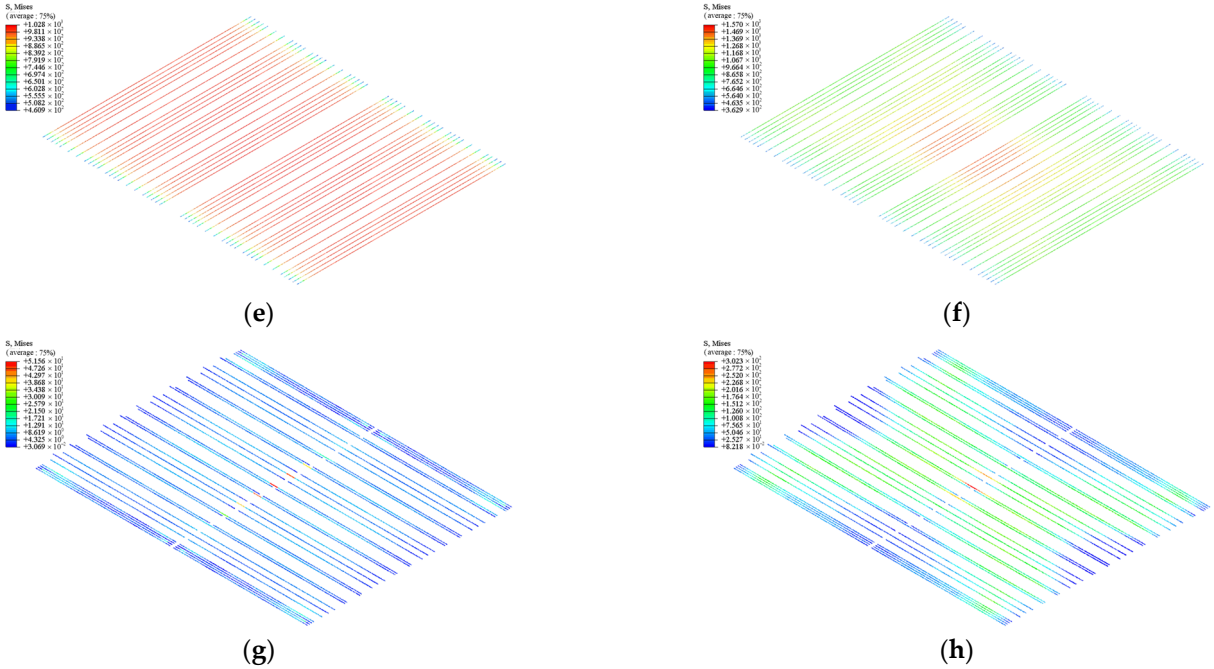


Figure 15. Analysis results of double-spliced composite bidirectional slab: (**a**) Deflection at cracking; (**b**) Deflection at failure; (**c**) Initial bottom cracks at cracking; (**d**) Distribution of bottom cracks at failure; (**e**) Stress in prestressing steel at cracking; (**f**) Stress in prestressing steel at failure; (**g**) Stress of transverse rebar stress at cracking; (**h**) Stress of transverse rebar stress at failure.

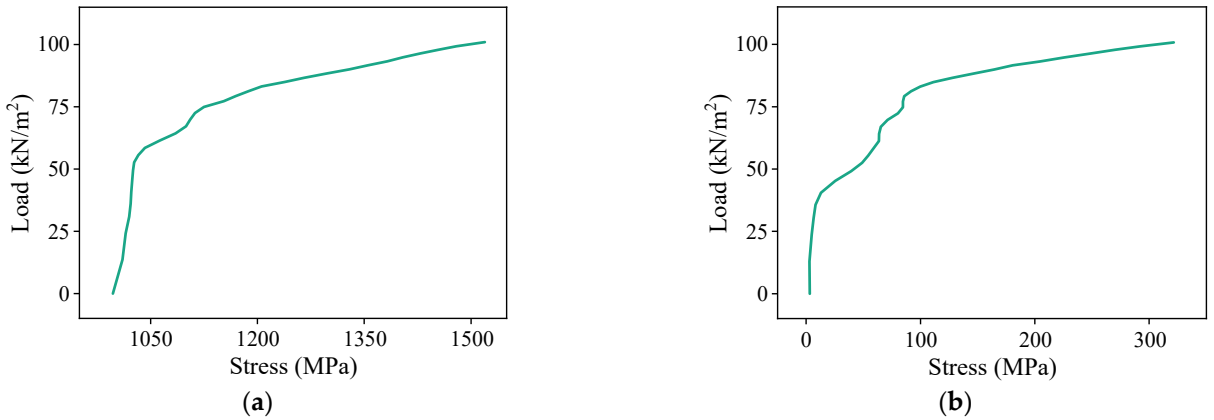


Figure 16. Load–stress curves for reinforcement at the center of the slab: (**a**) Prestressing steel; (**b**) Joint-connecting rebar.

5.2. Triple-Spliced Composite Bidirectional Slab

Figure 17a,c,e,g show the deflection of the double-spliced composite bidirectional slab, the distribution of cracks on the bottom surface, and the stress in the prestressing steel at the cracking load of 51.374 kN/m^2. The mid-span deflection is 1.181 mm. Cracks initially appear at the center of the slab and extend in the transverse direction parallel to the long edge of the slab. The stress in the prestressed steel is approximately 1030 MPa with a uniform distribution. The stress in the transverse rebars demonstrates a concentration at the joints at the third-point locations, with a maximum value of 45.82 MPa. Figure 17b,d,f,h depict the corresponding behaviors at the failure load of 96.555 kN/m^2, slightly lower than that of the double-spliced composite bidirectional slab. The mid-span deflection at failure, which is 14.88 mm, is comparable to that of the double-spliced composite bidirectional slab. The crack distribution on the bottom surface is similar to that of the double-spliced composite bidirectional slab, with a checkerboard pattern near the mid-span and extending

diagonally toward the corners. The prestressing steel near the center of the slab has yielded, resulting in the failure of the slab. The maximum stress of the transverse rebars occurs in the full-length rebars crossing the joints at the third-point joint locations, measuring 304.4 MPa. The other short rebars in the precast slab are at lower stress levels, most below 200 MPa.

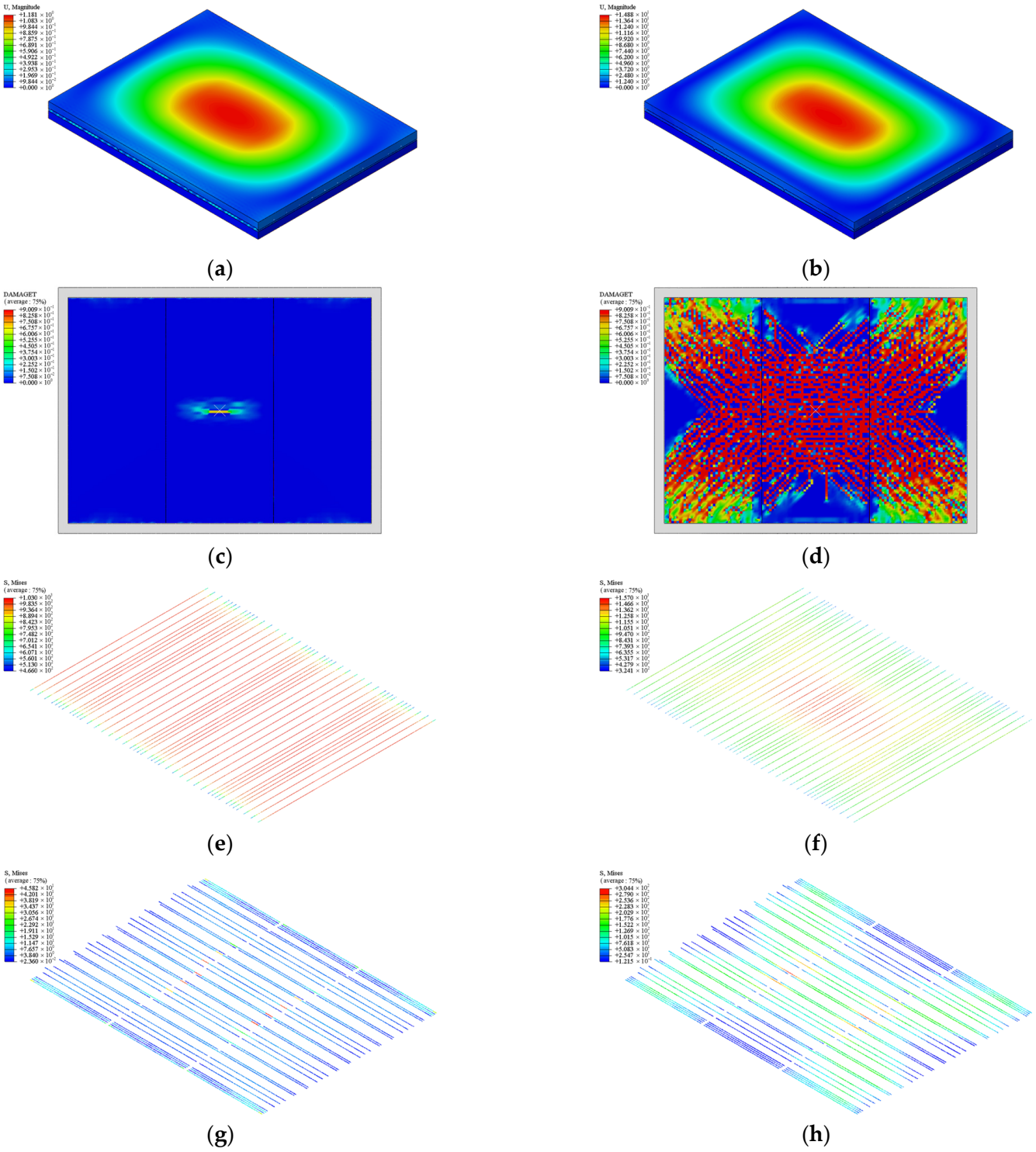


Figure 17. Analysis results of triple-spliced composite bidirectional slab: (**a**) Deflection at cracking; (**b**) Deflection at failure; (**c**) Initial bottom cracks at cracking; (**d**) Distribution of bottom cracks at failure; (**e**) Stress in prestressing steel at cracking; (**f**) Stress in prestressing steel at failure; (**g**) Stress of transverse rebar stress at cracking; (**h**) Stress of transverse rebar stress at failure.

Figure 18a,b illustrate the load–stress curves of the prestressed steel and the joint-connecting rebar at the center of the slab. When the load reaches about 50 kN/m^2, the stress in the prestressing steel begins to develop rapidly due to concrete cracking in the transverse direction, which is consistent with the double-spliced composite slab. In contrast, for the joint-connecting rebars, the load–stress curve shows a turning point at 65 kN/m^2, significantly higher than that observed in the double-spliced composite bidirectional slab. Furthermore, the maximum stress of the transverse joint-connecting rebars is much lower at the center of the slab, which is only about 130 MPa. This is attributed to the monolithic nature of the concrete at the slab's center, indicating that joint position is critical to the stress distribution of the transverse reinforcement.

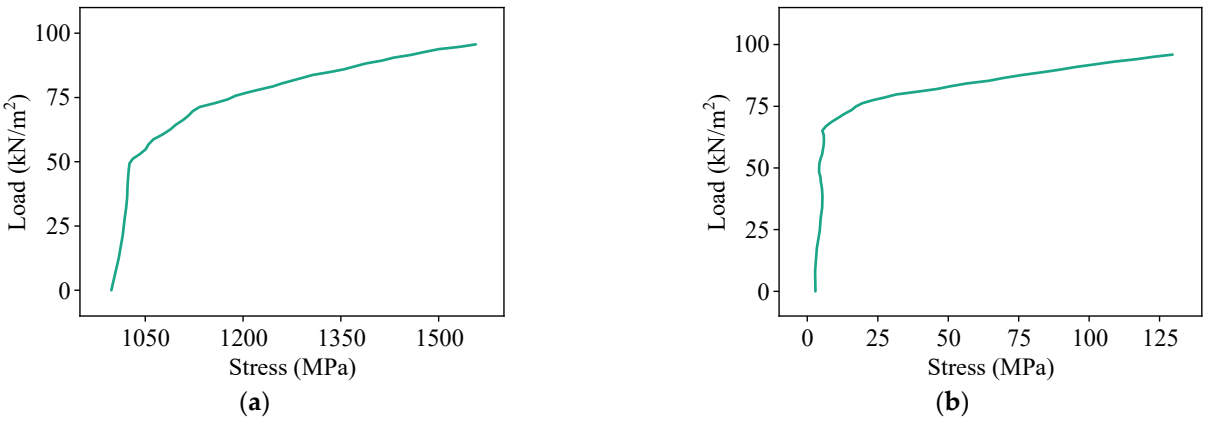


Figure 18. Load–stress curves for reinforcement at the center of the slab: (**a**) Prestressing steel; (**b**) Joint-connecting rebar.

5.3. Cast-in-Place Monolithic Bidirectional Slab

Figure 19a,c,e,g show the deflection of the double-spliced composite bidirectional slab, the distribution of cracks on the bottom surface, and the stress in the prestressing steel of the slab of the cast-in-place bidirectional loading slab when cracking occurs. The cracking load is 52.538 kN/m^2, with a corresponding mid-span deflection of 1.204 mm. Cracks initially appear near the center of the slab, with a tendency to develop diagonally toward the four corners. In this area, the stress in the prestressed steel and transverse rebars is approximately 1028 MPa and 27.88 MPa, respectively. Figure 19b,d,f,h depict the corresponding behaviors of the slab at the failure. The ultimate load is 99.789 kN/m^2, with a mid-span deflection of 13.81 mm. The crack distribution on the bottom surface is basically consistent with those of the double-spliced and triple-spliced composite bidirectional slabs. The prestressing steel near the center of the slab has yielded, while the maximum stress of the transverse rebars reaches 252.6 MPa.

Figure 20a,b illustrate the load–stress curves for the prestressing steel and the transverse rebars at the center of the slab. The turning points of both curves occur at an applied load of approximately 60 kN/m^2, signifying a balanced force transfer in both the longitudinal and transverse directions.

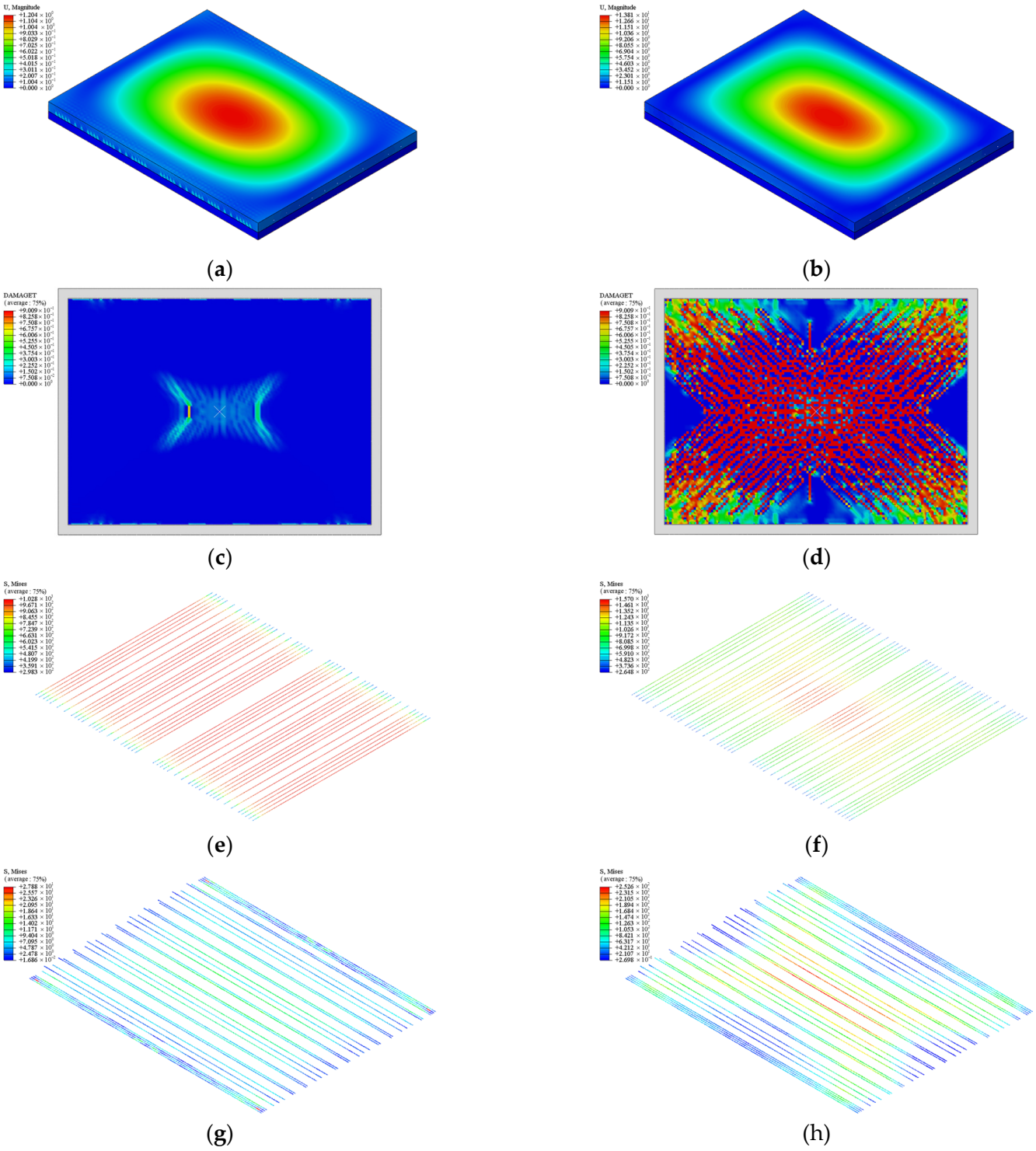


Figure 19. Analysis results of the cast-in-place bidirectional slab: (**a**) Deflection at cracking; (**b**) Deflection at failure; (**c**) Initial bottom cracks at cracking; (**d**) Distribution of bottom cracks at failure; (**e**) Stress in prestressing steel at cracking; (**f**) Stress in prestressing steel at failure; (**g**) Stress of transverse rebar stress at cracking; (**h**) Stress of transverse rebar stress at failure.

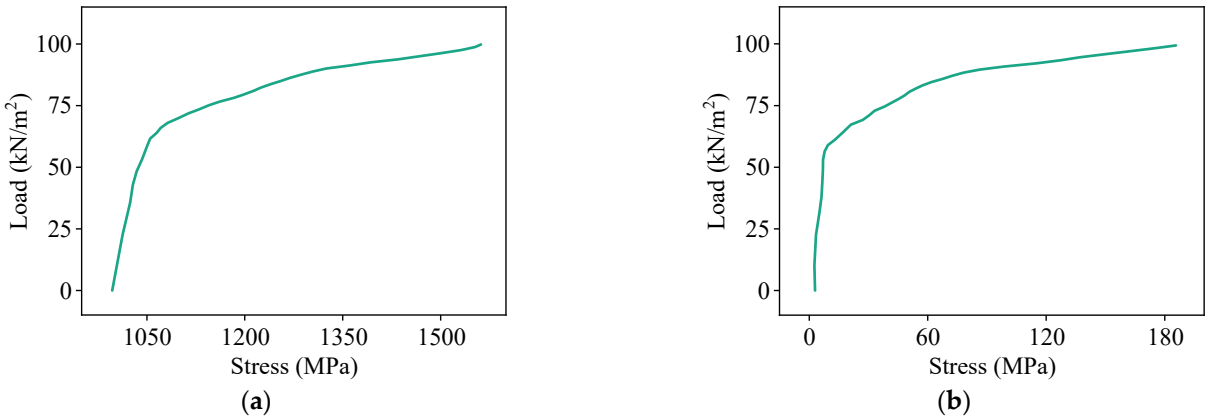


Figure 20. Load–stress curves for reinforcement at the center of the slab: (**a**) Prestressing steel; (**b**) Joint-connecting rebar.

5.4. Discussion of Results

Figure 21 presents the load–deflection curves for the double-spliced composite slab, triple-spliced composite slab, and the cast-in-place monolithic slab under bidirectional loading. The loading behavior of the slabs can be categorized into five distinct stages: the decompression state, elastic state, incipient cracking state, diagonal cracking state, and fully cracked state. In the initial decompression stage, the camber effect induced by prestressing is completely counteracted, bringing the deflection of the slabs to a condition equivalent to the starting state of non-prestressed members. Subsequently, as the load increases, the slabs transition into the elastic stage, exhibiting high stiffness with no damage. It can be seen that all the slabs demonstrate comparable stiffness during the elastic phase prior to cracking. Upon reaching the incipient cracking stage, transverse cracks begin to form perpendicular to the direction of the prestressed steel, leading to a gradual reduction in stiffness. The cracking loads of the double-spliced composite slab, the triple-spliced composite slab, and the cast-in-place monolithic slab are at similar levels, 53.701, 51.374, and 52.538 kN/m^2, respectively. As diagonal cracks initiate and propagate, the stiffness further diminishes, eventually stabilizing in the final, fully cracked state. Compared with unidirectional loading conditions, the cracking load and bearing capacity of the double-spliced and triple-spliced bidirectional composite slabs both have great improvements, by more than 60%. The double-spliced composite slab and the cast-in-place monolithic slab exhibit a similar response and failure load. However, there are some differences in the crack propagation and post-crack stiffness between the composite and monolithic slabs. Due to the existence of the splicing joints in composite slabs, the overall integrity is reduced and the diagonal cracking is slightly delayed compared with the monolithic slab. Therefore, the post-crack stiffness of the double-spliced composite slab is slightly lower than that of the monolithic slab during the early stage of cracking, but the difference diminishes after cracks have fully developed. For the triple-spliced composite slab, its response is softer as a result of a marginally lower ratio of the prestressing steel, with decreases of 3.24% and 4.68% for failure load compared with the cast-in-place slab and double-spliced composite slab, respectively. In terms of ultimate mid-span deflection, the double-spliced and triple-spliced composite slabs exhibit values of 14.85 mm and 14.88 mm, respectively. These deflections are 7.53% and 7.75% greater than that of the cast-in-place slab, which measures 13.81 mm. This indicates that the presence of splicing joints slightly reduces the overall structural integrity of the slabs; however, the arrangement of the joints has a negligible impact on serviceability. Overall, all three bidirectional slabs demonstrate excellent ductility throughout the loading process.

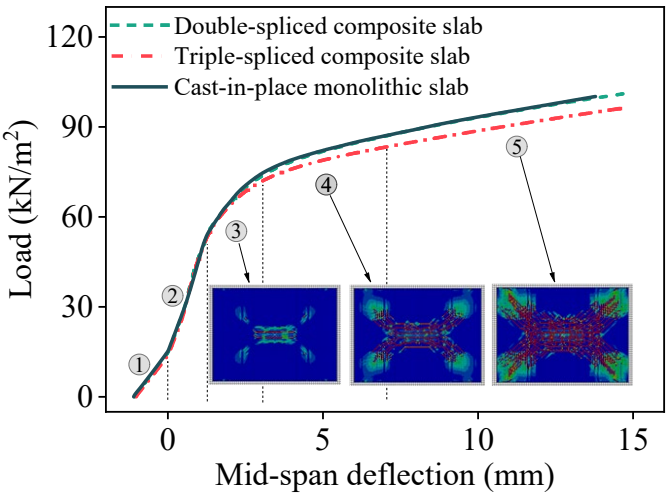


Figure 21. Load–deflection curves for bidirectional slabs.

The failure of all three slabs is initiated by the yielding of the longitudinal prestressing steel oriented parallel to the short edge of the bidirectional loading slab. To incorporate more failure modes and investigate the influence of major factors, parametric analysis was conducted regarding the ratio of prestressing steel, concrete strength, strength, and diameter of the joint-connecting rebars. The thickness and space of the steel ribs were not involved in the parametric analysis because previous studies [26] have shown that the steel ribs mainly enhance the stiffness during construction and have a very limited contribution after composition. Figure 22 illustrates three possible failure modes for dense splicing slabs, as shown in the following: (1) yielding of the longitudinal prestressing steel; (2) concrete crushing; (3) joint failure, i.e., yielding of the transverse joint-connecting steel.

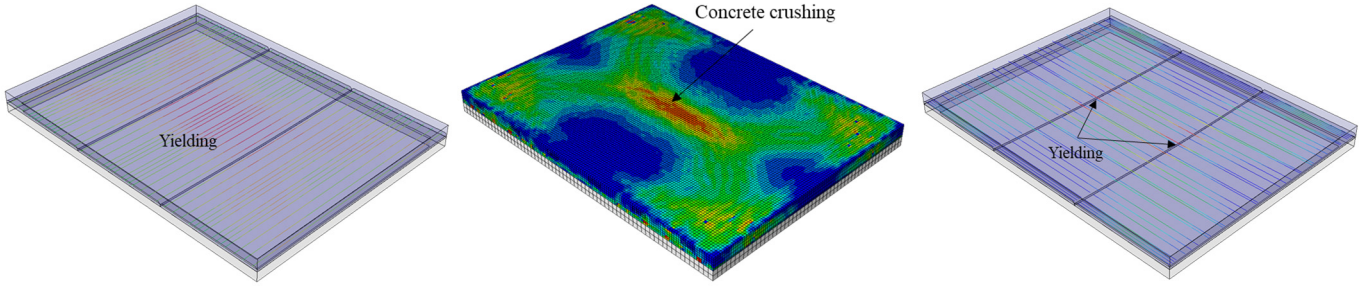


Figure 22. Failure modes of dense splicing slabs: (**a**) Yielding of the longitudinal prestressing steel; (**b**) Concrete crushing; (**c**) Yielding of the transverse joint-connecting steel.

In view of the similarity of the bidirectional behavior of the double-spliced and triple-spliced composite slabs, only the analysis results of the triple-spliced composite slab are presented here, as illustrated in Figure 23. Failure labels P, C, and J, marked at the end of each curve, represent the above failure modes 1–3, respectively. As can be seen from Figure 23, the ratio of the longitudinal prestressing steel has the most significant effect on the behavior of the slab, followed by the concrete strength. The influence of the strength and diameter of the joint-connecting rebar are very limited and even can be negligible. In the range of the prestressing steel ratio from 0.072% to 0.394%, the failure modes are all controlled by the yielding of the prestressing steel, with the ultimate bearing capacity basically proportional to the increase in the prestressing steel ratio. Regarding the concrete strength, its effect on the improvement in the bearing capacity gradually decreases with the increase in concrete grade, especially after C40. For the bidirectional slab made of C20

concrete, the concrete is close to collapse when the prestressed tendons yield, while the failure criteria for C30, C40, and C50 are only the yielding of the longitudinal prestressing steel. For the strength of the joint-connecting rebars lower than 235 MPa, or the diameter smaller than 4 mm, the joint failure will occur under bidirectional loading, decreasing the ultimate bearing capacity and ductility of the slabs. However, for other conditions of joint-connecting rebars, their performances are basically identical.

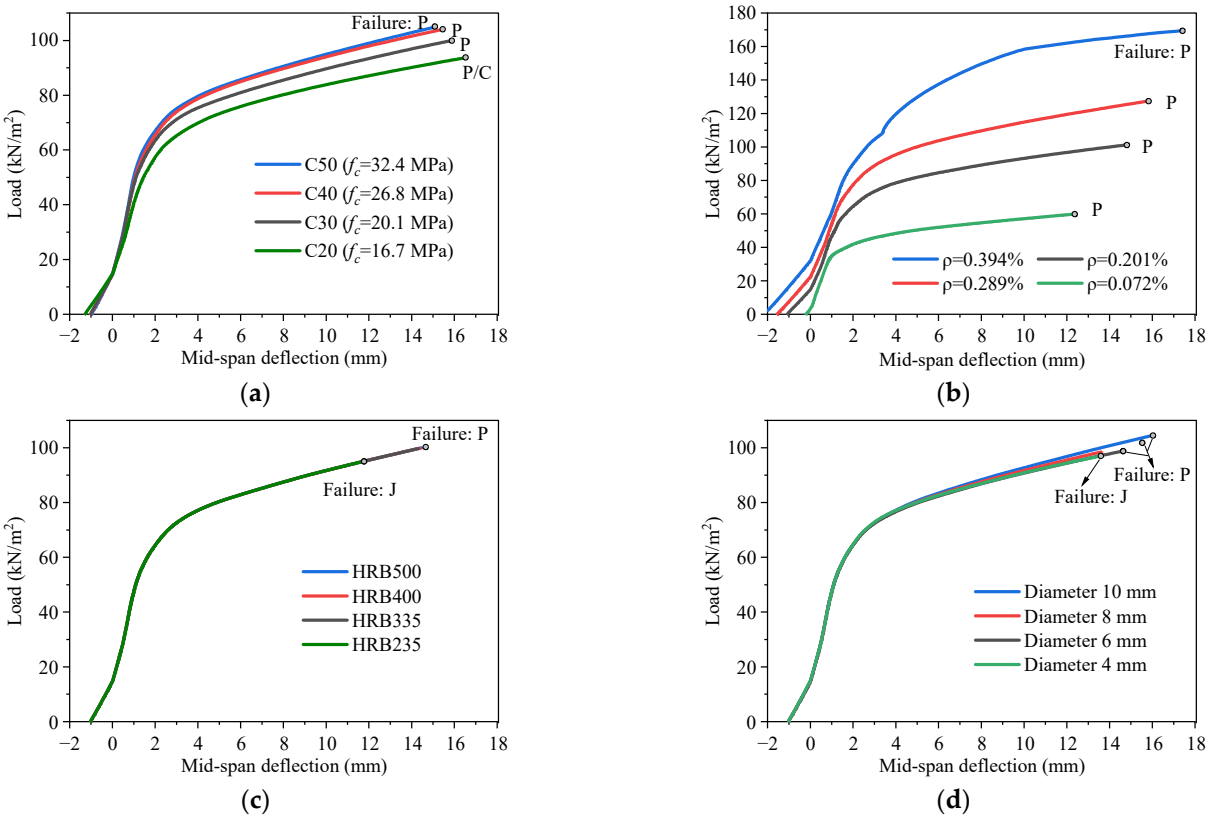


Figure 23. Parametric analysis results of the triple-spliced composite slab: (**a**) Concrete strength; (**b**) Ratio of the longitudinal prestressing steel; (**c**) Strength of the joint-connecting rebar; (**d**) Diameter of the joint-connecting rebar.

6. Conclusions

This study examines the unidirectional and bidirectional bending performance of prestressed concrete composite slabs with steel ribs for substation applications. The following conclusions are drawn:

(1) For unidirectional bending performance, the designed composite slabs present typical two-stage load-bearing characteristics, with concrete cracking as the turning point. The post-crack stiffness of the composite slabs remains relatively stable until failure. The cracks on the bottom surface are predominantly transverse and uniformly distributed from mid-span toward the supports, with localized cracks along the steel ribs. The ultimate capacity of the slab depends on the yielding of the prestressing steel. The numerical simulation results align closely with theoretical calculations, with errors within 7.76%, thereby validating the accuracy of the FE models.

(2) For bidirectional bending performance, the loading behavior of the composite and monolithic slabs can be categorized into five distinct stages: the decompression state, elastic state, incipient cracking state, diagonal cracking state, and fully cracked state. All the slabs demonstrate comparable stiffness prior to cracking and similar crack distributions at failure, with a checkerboard pattern near the mid-span and extending

diagonally toward the slab corners. The presence of splicing joints reduces the post-crack stiffness slightly and increases the ultimate deflections of the double-spliced and triple-spliced composite slabs, which are 7.53% and 7.75% greater than that of the monolithic slab, respectively. Nonetheless, the ultimate capacities remain close to that of the cast-in-place slab.

(3) The parametric analysis shows that the longitudinal prestressing steel ratio has the most significant effect on the behavior of the bidirectional slab, with the ultimate bearing capacity increasing in proportion to the prestressing steel ratio from 0.072% to 0.394%. The beneficial effect of the increase in concrete strength on the bearing capacity gradually decreases, especially after C40. When the arrangement of the joint-connecting rebars greater than C4 @ 200 mm with a minimum yield strength of 235 MPa, the transversal force transfer across the joints is reliable.

(4) The new type of prestressed concrete composite slabs with steel ribs introduced in this study features high cracking strength, stiffness, load-bearing capacity, and commendable ductility under both unidirectional and bidirectional loading conditions, making it highly appropriate for substation applications. For different substation sizes, the ratio of the prestressing steel should be adjusted to meet the capacity requirements. For a larger room space, a grid of secondary beams can be set beneath the floor slabs to form a two-way slab system to obtain a higher bending performance.

Author Contributions: Conceptualization, methodology, and writing—original draft preparation, L.L. and Y.L.; investigation and formal analysis, Z.W. and Y.J.; software and data curation, H.C.; supervision and writing—review and editing, Y.Z.; validation, C.L.; resources and project administration, K.R. and L.T. All authors have read and agreed to the published version of the manuscript.

Funding: This research received no external funding.

Data Availability Statement: The datasets generated and/or analyzed during the current study are available from the corresponding author upon reasonable request.

Conflicts of Interest: Authors Lin Li, Yong Liu, Zhenzhong Wei, and Yunan Jiang were employed by Shandong Electric Power Engineering Consulting Institute Co., Ltd. The remaining authors declare that the research was conducted in the absence of any commercial or financial relationships that could be construed as a potential conflict of interest.

References

1. Luo, T.; Xue, X.L.; Wang, Y.N.; Xue, W.R.; Tan, Y.T. A systematic overview of prefabricated construction policies in China. *J. Clean Prod.* **2021**, *280*, 124371. [CrossRef]
2. Bonamente, E.; Cotana, F. Carbon and energy footprints of prefabricated industrial buildings: A systematic life cycle assessment analysis. *Energies* **2015**, *8*, 12685–12701. [CrossRef]
3. Bai, S.; Li, M.C.; Song, L.G.; Kong, R. Developing a common library of prefabricated structure components through graphic media mapping to improve design efficiency. *J. Constr. Eng. Manag.* **2021**, *147*, 04020156. [CrossRef]
4. Jiang, Y.; Shu, J.P.; Ye, J.; Zhao, W.J. Virtual trail assembly of prefabricated structures based on point cloud and BIM. *Autom. Constr.* **2023**, *155*, 105049. [CrossRef]
5. He, H.; Zhou, S.; Zhang, L.; Zhao, W.; Xiao, X. Dynamic accounting model and method for carbon emissions on the power grid side. *Energies* **2023**, *16*, 5016. [CrossRef]
6. Li, C.Z.; Chen, Z.; Zhao, Y.Y.; Zhou, M.Z.; Zhang, L.M. Design and Application of Prefabricated Substation Based on BIM Technology. In Proceedings of the 24th International Symposium on Advancement of Construction Management and Real Estate, Chongqing, China, 29 November–2 December 2021. [CrossRef]
7. Zhao, Y.Y.; Li, R.; Yue, S.Y. Comparative Analysis of Modular Prefabricated Module Substation and Conventional Substation. In Proceedings of the 3rd International Conference on Cognitive based Information Processing and Applications, Guangzhou, China, 2–3 November 2023. [CrossRef]
8. Shen, Q.S.; Sheng, X.H.; Jiang, X.Y.; Wu, L.; Sheng, S.Y. Design research and engineering application of substation assembled fence and firewall. *Zhejiang Electr. Power* **2014**, *33*, 28–33. [CrossRef]

9. Li, T.; Guo, J.; Hu, S.Y.; Chai, L.J.; Jing, Z.P.; Cheng, R.; Wang, Z.L. Research on the design of the integrated wall panel of the prefabricated building in substations. *J. Phys. Conf. Ser.* **2021**, *1904*, 012026. [CrossRef]
10. Hou, G.R.; Wang, X.X.; Lu, N.N.; Xie, J.G.; Huang, G. Experimental study on seismic behavior of new prefabricated partial SRC frame beam-column joints. *Build. Struct.* **2018**, *48*, 27–32. [CrossRef]
11. Liu, Y.; Wei, Z.Z.; Zhen, Y.C.; Jiao, J.F. Application exploration and practice of prestressed steel pipe truss floor slab in substation. *Shandong Electr. Power* **2021**, *48*, 39–43.
12. Yu, J.H.; He, M.J.; Zhang, S.H.; Zhao, Y.Y.; Tang, Y.X. Experimental study on the mechanical behavior of prestressed concrete steel pipe truss composite slabs under the influence of secondary force. *Build. Struct.* **2021**, *51*, 80–85. [CrossRef]
13. Huang, H.L.; Wu, F.B.; Zhu, M.Q.; Zeng, C.; Lv, W. Influence of rib details on flexural behavior of concrete composite slab with precast prestressed ribbed pane. *J. Build. Struct.* **2015**, *36*, 66–72. [CrossRef]
14. Liu, J.P.; Hu, H.F.; Li, J.; Chen, Y.F.; Zhang, L. Flexural behavior of prestressed concrete composite slab with precast inverted T-shaped ribbed panels. *Eng. Struct.* **2020**, *215*, 110687. [CrossRef]
15. Hou, H.T.; Liu, X.; Qu, B.; Ma, T.; Liu, H.; Feng, M.; Zhang, B. Experimental evaluation of flexural behavior of composite beams with cast-in-place concrete slabs on precast prestressed concrete decks. *Eng. Struct.* **2016**, *126*, 405–416. [CrossRef]
16. Karimipanah, A.; Zeynalian, M.; Ataei, A. Structural performance of cold formed steel composite beams with profiled steel sheeting. *Int. J. Civ. Eng.* **2024**, *22*, 1099–1116. [CrossRef]
17. Lei, X.S.; Ouyang, J.W.; Wang, Y.F.; Wang, X.H.; Zhang, X.F.; Chen, F.; Xia, C.; Liu, Z.; Zhou, C.Y. Thermal–Mechanical Coupling Evaluation of the Panel Performance of a Prefabricated Cabin-Type Substation Based on Machine Learning. *Fire* **2021**, *4*, 93. [CrossRef]
18. Wang, G.S.; Liu, J.H.; Zhang, Y.B.; Zhang, Z.Y.; Tao, J.W.; Wu, D.Y. Theoretical and experimental study on the stress state of joints in two-way composite slabs. *Buildings* **2024**, *14*, 3374. [CrossRef]
19. Li, J.; Ni, D.Y.; Liu, X.; Zhang, J.R. Experimental study of mechanical properties of L-shaped joint laminated two-way slabs. *Build. Struct.* **2020**, *50*, 67–71. [CrossRef]
20. Cheng, Z.J.; Ma, Z.Z.; Hu, J.; Yu, S.L.; Zhao, Y. Experimental research on heap loading of reinforced concrete composite two-way slab with lattice girders and connected without gap. *Build. Struct.* **2021**, *51*, 111–119. [CrossRef]
21. Chen, Y.H.; Lu, D.; Zhang, M.; Sun, H.W.; Xie, G.X. Research on connection technique for bidirectional composite floor slabs without gap. *Ind. Constr.* **2020**, *50*, 31–35. [CrossRef]
22. *T/CECS 1289-2023*; Technical Specification for Prestressed Concrete Composite Slab with Steel Ribs. China Association for Engineering Construction Standardization: Beijing, China, 2023.
23. Abaqus. *Computer Software*, Version 6.14; SIMULIA: Providence, RI, USA, 2014.
24. Hou, H.T.; Feng, M.Y.; Qiu, C.X.; Lan, R.H.; Qu, B.; Wang, Y.M.; Tian, L. Experimental study and numerical simulation on prestressed concrete composite slab with steel ribs. *Build. Struct.* **2018**, *39*, 103–110.
25. *GB 50010-2010*; Concrete Structure Design of Concrete Structures. Ministry of Housing and Urban-Rural Development of the People's Republic of China: Beijing, China, 2012.
26. Chen, X.; Li, H.S.; Gao, M.Q.; Sun, J.G.; Hou, H.T. Experimental study and numerical simulation on prestressed concrete composite slab with steel ribs. *Build. Struct.* **2021**, *51*, 98–103+60.

Disclaimer/Publisher's Note: The statements, opinions and data contained in all publications are solely those of the individual author(s) and contributor(s) and not of MDPI and/or the editor(s). MDPI and/or the editor(s) disclaim responsibility for any injury to people or property resulting from any ideas, methods, instructions or products referred to in the content.